Joint Numerical and Experimental Investigation of Roughness Effect on Hypersonic 2nd Mode Instability and Transition

Christopher Haley*
University of California, Los Angeles, CA 90095, USA
Katya M. Casper†
Sandia National Laboratories, Albuquerque, NM 87185, USA
and Xiaolin Zhong‡
University of California, Los Angeles, CA 90095, USA

This paper details a joint numerical and experimental investigation of transition-delaying roughness. A numerical simulation was undertaken to design a surface roughness configuration that would suppress Mack's 2nd mode instability in order to maintain laminar flow over a Mach 8 hypersonic blunt cone. Following the design process the roughness configuration was implemented on a hypersonic cone test article. Multiple experimental runs at the Mach 8 condition with different Reynolds numbers were run, as well as an off-design Mach 5 condition. The roughness did appear to delay transition in the Mach 8 case as intended, but did not appear to delay transition in the Mach 5 case. Concurrently, simulations of the roughness configuration were also computed for both Mach cases utilizing the experimental conditions. Linear stability theory was applied to the simulations in order to determine their boundary layer stability characteristics. This investigation of multiple cases helps to validate the numerical code with real experimental results as well as provide physical evidence for the transition-delaying roughness phenomenon.

I. Introduction

This paper presents a joint numerical and experimental investigation of transition-delaying roughness. Hypersonic vehicles are often subjected to severe drag and surface heating when operating in high Mach number flow regimes. In order to survive flight, structurally heavy thermal protection system (TPS) are necessary. High speed boundary layer transition research has made considerable progress in recent decades towards understanding the mechanisms behind transition,[1,2] especially the identification of Mack's 2nd mode as the dominant instability within the hypersonic boundary layer.[3] As a result, several boundary layer control strategies have been devised in order to mitigate the severity of boundary layer transition. One such strategy is Zhong and Fong's passive hypersonic laminar flow control which uses finite height spanwise roughness strips to delay the onset of transition.[4] This transition-delaying roughness phenomenon was unexpectedly observed nearly 60 years ago in two separate experiments, with little explanation of its cause.[5,6] A more recent experiment performed by Fujii also showed evidence of the transition-delaying roughness phenomenon.[7] Duan and Zhong found that the placing discrete surface roughness downstream of the synchronization location of Mack's 2nd mode acted to suppress the instability.[8] Since then the phenomenon has been studied extensively by Fong and Zhong with numerical simulations of 2-D roughness elements on a flat plate.[9,10] Culminating in the application of their laminar flow control strategy to a validation experiment on a compression cone.[11] The objective of this paper is to provide a complete validation study between simulation and experiment of a transition-delaying roughness array on a blunt cone as well as provide additional physical evidence of the phenomenon.

*Graduate Research Assistant, Mechanical and Aerospace Engineering Department, UCLA, clhaley@g.ucla.edu.
†Principal Member of the Technical Staff, Engineering Sciences Center, Senior Member AIAA.
‡Professor, Mechanical and Aerospace Engineering Department, UCLA, AIAA associate fellow.

In previous numerical simulations, it has been shown that placing 2-D roughness elements downstream of the synchronization location of Mack's 2nd mode instability will suppress the instability.[9,11] This numerical result was validated in Purdue's Mach 6 quite tunnel on a compression cone in which six rows of axisymmetric roughness elements were shown to suppress the 2nd mode around a frequency of 280 kHz; the most unstable frequency determined from N-factor analysis.[10] This experiment, however, was performed on a compression cone with a nearly constant boundary layer thickness for which there is only one 2nd mode instability frequency. A similar suppression result is not necessarily guaranteed for a straight cone with a growing boundary layer and multiple unstable frequencies like the cone featured in this paper.

In order to progress the understanding of the transition-delaying roughness effect, this paper details the design and execution of a 2-D roughness experiment on a straight cone in Sandia National Laboratories Mach 8 Hypersonic Wind Tunnel (HWT-8). The design of the transition-delaying roughness was carried out prior to the experiment with a numerical simulation of the test article and stability analysis of its meanflow.[12] The design is then implemented on the test article and the experiment is run. Several different freestream cases with the same roughness configuration are examined experimentally at Mach 8 and Mach 5. Originally the roughness array was designed for a cone with a 0.5 mm nose radius but was implemented on a test article with a 0.05 mm radius. Consequently, new numerical simulations are carried out at Mach 8 and Mach 5 with the same cone geometry and the same freestream conditions as the experiment.

II. Computational Methodology

The DNS code utilized in this paper is a 5th-order code that uses shock-fitting to accurately compute the location of the bow shock on a straight blunt cone geometry. This base geometry and high-order shock-fitting approach has been validated extensively for accuracy.[13] The roughness element is implemented by mapping an analytical shape to the conical surface geometry. By this approach, a high-order accuracy for the entire problem is maintained, making it suitable for unsteady simulations and analysis with linear stability theory (LST). The LST computations in this paper are based on Malik's spatial multi-domain spectral method.[14]

A. Governing Equations

The DNS code solves the conservation-law form of the three-dimensional Navier-Stokes equations in Cartesian coordinates. Written in vector form, the governing equations are

$$\frac{\partial U}{\partial t} + \frac{\partial F_j}{\partial x_j} + \frac{\partial F_{v,j}}{\partial x_j} = 0 \tag{1}$$

in which U is the state vector of conserved quantities, and F_j and $F_{v,j}$ are the inviscid flux and viscous flux in the j^{th} spatial direction respectively,

$$U = \{\rho,\ \rho u_1,\ \rho u_2,\ \rho u_3,\ e\}^T \tag{2}$$

$$F_j = \{\rho u_j,\ \rho u_1 u_j + p\delta_{1j},\ \rho u_2 u_j + p\delta_{2j},\ \rho u_3 u_j + p\delta_{3j},\ (e+p)u_j\}^T \tag{3}$$

$$F_{v,j} = \{0,\ \tau_{1j},\ \tau_{2j},\ \tau_{3j},\ \tau_{jk}u_k - q_j\}^T \tag{4}$$

The internal energy, e, shear stress, τ_{ij}, and heat flux, q_j, are given as follows,

$$e = \rho\left(c_v T + \frac{u_k u_k}{2}\right) \tag{5}$$

$$\tau_{ij} = \mu\left(\frac{\partial u_i}{\partial x_j} + \frac{\partial u_j}{\partial x_i}\right) + \delta_{ij}\lambda\frac{\partial u_k}{\partial x_k} \tag{6}$$

$$q_j = -\kappa\frac{\partial T}{\partial x_j} \tag{7}$$

To close Eq. (1), a calorically perfect gas is assumed. For the simulations under consideration, the properties of nitrogen gas at Mach 8 and air at Mach 5 are used. This is consistent with the experimental conditions. Lastly, the viscosity, μ, is calculated using Sutherland's law.

Equation (1) is solved in a physical domain defined between the bow shock and cone surface. The bow shock location is solved using a high-order shock-fitting method, where the transient shock movement is

solved as an ODE alongside the governing equation. Within the physical domain a curvilinear grid defines a computational domain. A solution to Eq. (1) is computed by transforming the governing equations to the computational domain. The transformed equations are discretized using a 5^{th}-order finite difference stencil in space and integrated using Euler's method (RK-1). Details of the high-order finite difference schemes can be found in Zhong, 1998.[13]

B. Discrete Body-fitted Roughness

The surface roughness elements in this paper are implemented by mapping the difference of two hyperbolic tangents to the frustum of a cone. This body-fitted roughness approach requires that the roughness function be compatible with the aforementioned grid transformation between the physical and computational domains. For multiple axisymmetric strips the function is given as:

$$y'(x', z') = \frac{1}{2}\sum_{i=1}^{N} h_i \left\{ \tanh\left[q\left((x' - l_i) + \frac{w_i}{2} \right) \right] - \tanh\left[q\left((x' - l_i) - \frac{w_i}{2} \right) \right] \right\} \tag{8}$$

where x', y', and z' are Cartesian coordinates prior to being mapped to the cone surface. The parameters h_i, w_i and l_i control the height, width and location of an individual roughness strip and q is a free parameter that controls the edge steepness. Equation (8) is mapped to the cone's frustum using the following rotation and translation equations,

$$\begin{aligned} x &= cos(\theta_{\frac{1}{2}})x' - sin(\theta_{\frac{1}{2}})y' + x_c \\ y &= [sin(\theta_{\frac{1}{2}})x' + cos(\theta_{\frac{1}{2}})y' + y_c]cos(\phi) \\ z &= [sin(\theta_{\frac{1}{2}})x' + cos(\theta_{\frac{1}{2}})y' + y_c]sin(\phi) \end{aligned} \tag{9}$$

in which x, y, and z are the Cartesian coordinates in the physical domain, $\theta_{\frac{1}{2}}$ is the cone half-angle, ϕ is the angle in the azimuthal direction about the cone, and x_c and y_c is the surface location of the first roughness strip. Figure 1 plots Eq. (8) as it would appear on a cone frustum after applying Eq.(9). Figure 1 is also the roughness array configuration implemented in this paper for both Mach 8 and Mach 5 simulations.

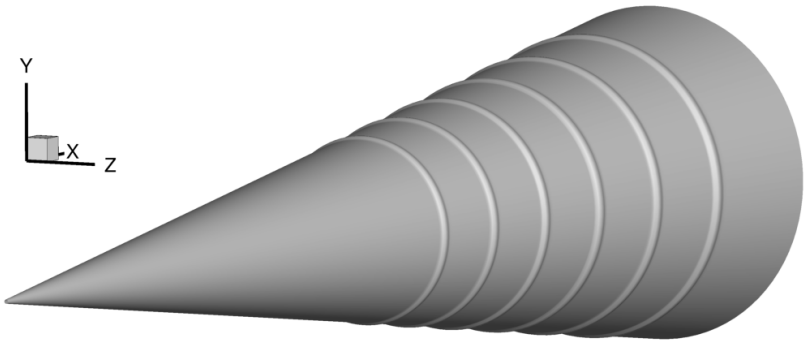

Figure 1: Roughness array generated after mapping Eq. (8) to cone frustum for six strips with $q = 2000$.

C. Simulation Conditions

Two new simulations cases are presented in this paper: a Mach 8 and Mach 5 case. These cases were computed after the design and experimental implementation of the roughness-array described in section 4. For that reason their freestream conditions and cone geometries were taken from the experimental results. In this way the numerical results can be more accurately validated from experiment. The simulation conditions are listed in Table 1 below. For both cases the cone is straight with a 7° half-angle and is 0.532 m in length.

Table 1: Simulation conditions for Mach 8 & 5 cases

Parameter	Mach 8 Case	Mach 5 Case	Unit
M_∞	7.84	4.96	-
ρ_∞	0.022455	0.055751	kg/m^3
p_∞	344.442	1297.27	Pa
T_∞	51.68	81.08	K
T_w	279.0	279.0	K
r_n	0.05	0.5	mm

III. Experimental Methodology

A. Sandia Hypersonic Wind Tunnel

Experiments were performed in the Sandia Hypersonic Wind Tunnel (HWT). The tunnel is a conventional blowdown-to-vacuum facility. Interchangeable nozzle and heater sections allow the tunnel to be run at Mach 5, 8 or 14. Experiments are conducted only at Mach 5 and 8 for the present work. Run times were typically 30 s. HWT-5 uses air as the driver gas. It has a P_0 range of 345–1380 kPa and a T_0 range of 330–890 K, giving a Re range of 3.3–26 $\times 10^6/m$. Noise levels vary from 1–2% in this tunnel.[15] HWT-8 uses 689 MPa nitrogen supplied from a bottle farm. It has a P_0 range of 1720–6890 kPa, T_0 range of 500–890 K, and Re can be varied from 3.3–20 $\times 10^6/m$. Noise levels vary from 3–5%.[15] Run conditions for the cases shown here are presented in Table 2.

Table 2: Experimental Run Conditions

Case	Re $\times 10^6/m$	M_∞	P_o (kPa)	T_o (K)	Roughness
1	7.0	7.8	2924	697	No
2	7.2	7.8	2950	687	Yes
3	8.6	7.9	3189	644	No
4	9.0	7.9	3230	630	Yes
5	8.8	5.0	655	480	Yes
6	9.4	5.0	683	472	No

B. Model and Instrumentation

A 0.517-m-long 7° half-angle stainless-steel cone was used for the present work (Fig. 2). This model is the same as that used in previous experimental campaigns that were focused on better understanding fluid-structure interactions in hypersonic flow.[16]

The boundary layer state was characterized by PCB132 pressure sensors at x = 0.422 and 0.497 m from the sharp nosetip. These sensors are very high frequency piezoelectric time-of-arrival sensors that can be used to measure pressure fluctuations between 11 kHz and 1 MHz. This high frequency response allows a study of instability breakdown to transition on the cone (typically near 200 kHz) and is a useful indicator of transition on the model. The PCB132 sensor signals connect to a PCB 482A22 signal conditioner that provides constant-current excitation to the built-in sensor amplifier. It also decouples the AC signal from the DC bias voltage. The output from the signal conditioner is fed through a Krohn-Hite Model 3944 Filter with a 1.25 MHz low-pass anti-aliasing Bessel filter. This filter has four poles and offers 24 dB of attenuation per octave. The sampling frequency for the PCB132 signals was 2.5 MHz. Pressure sensor data were acquired using a National Instruments PXI-1042 chassis with 14-bit PXI-6133 modules (10 MHz bandwidth).

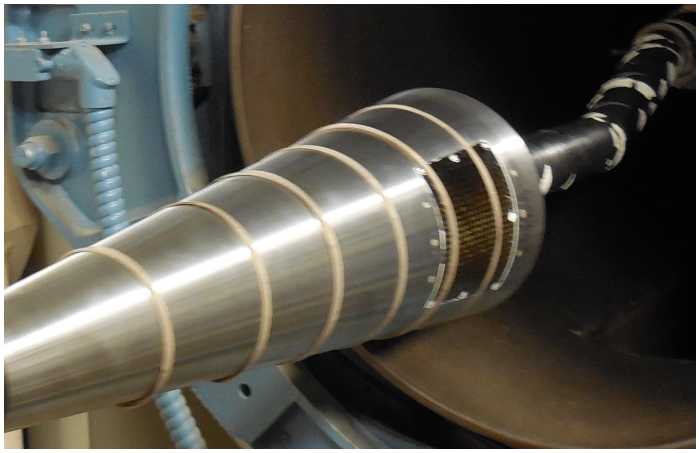

Figure 2: Wind-tunnel model with roughness strips in the Sandia Hypersonic Wind Tunnel.

A high-speed schlieren system was also used to take movies at 200 kHz of the boundary layer between x = 0.422 and 0.497 m while also being able to resolve the detailed structure of the boundary-layer disturbances. The design and implementation of this system is discussed in detail in Ref. 17 and is therefore only briefly discussed here. Fig. 3 shows a simple schematic of the system. A Cavilux Smart Laser was used as the light source, in place of the Flashpoint II Monolight that had been used in previous setups. The light from the source was passed through a slit to increase sensitivity. Two 101.6-mm diameter convex lenses with a 1-m focal length were then used to collimate the remaining light, pass it through the test section, and focus the light on a knife edge. The lenses were equally spaced on either side of the tunnel centerline. Most of the light was cut off at the knife edge to increase the sensitivity of the schlieren system. The remaining light was then captured by a Phantom v12.1 digital camera. The slit, knife edge, and camera were all tilted 7° from horizontal to align with the cone surface.

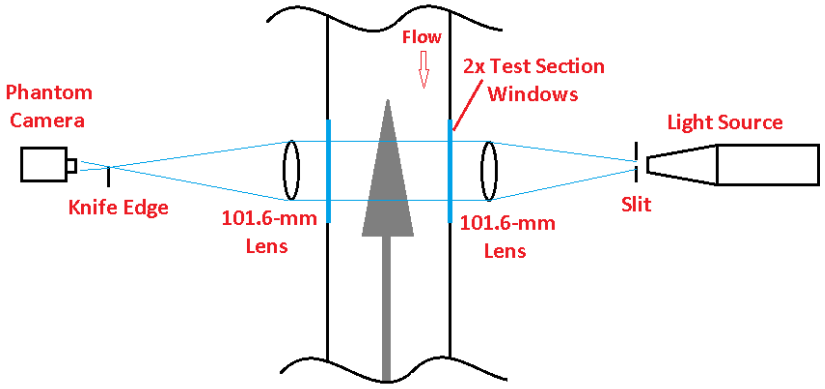

Figure 3: Schematic of the high-speed schlieren system for the Sandia Hypersonic Wind Tunnel.

IV. Roughness Design

The roughness elements in this paper are designed using a process patented by Zhong and Fong for passive hypersonic laminar flow control.[4] For a given meanflow, the process begins with identifying the frequency of Mack's 2nd mode instability most likely to start transition as determined by the empirical e^N method. This frequency is identified in one of several ways: by either knowing the transition location (or onset of intermittent turbulence) from experimentation, the N-value at which transition typically occurs, or by some other means. Next the so-called synchronization location—the location at which the phase speeds of mode F and mode S are the same—is determined for the identified frequency. This location is typically upstream of

where transition starts to occur. The boundary layer thickness at the synchronization location is determined next. The passive laminar flow strategy maintains that a roughness element placed at the synchronization location with a height less than the local boundary layer thickness will suppress the selected frequency as well as unstable frequencies higher than it. The control strategy goes on to state that a streamwise array of roughness strips is capable of suppressing all unstable frequencies, thus delaying transition indefinitely.

The roughness-array implemented in this paper was initially designed for a Mach 8 cone with a blunt nose radius of 0.5 mm. A simulation of the flowfield and design of a single transition-delaying roughness is detailed in Haley and Zhong.[12] The freestream conditions, blunt cone dimensions, and intermittent turbulence results were taken from a previous experimental case performed by Casper et al. in Sandia's HWT-8.[17] The single roughness strip design was modified to include multiple strips in order to suppress all unstable frequencies. The design of the single roughness strip and the array is described in the following subsections. In the execution of this joint numerical and experimental investigation, however, the expertimental test article used a nose radius of 0.05 mm. Since it is unclear how reducing the nose radius will effect the roughness-array's ability to suppress boundary layer instabilities, a simulation of the 0.05 mm nose radius cone at the experimental test conditions was computed. The stability analysis of the simulation in section 5 indicates that the as-designed roughness-array should be adequate in suppressing boundary layer transition.

A. Freestream conditions and simulation parameters

The numerical simulation used to design the roughness-array is based on a straight circular blunt cone with a 7° half-angle and a nose radius of 0.5 mm. The total simulation length is 0.534 m measured from the blunt nose tip. The simulation has no angle of incidence with the freestream. The freestream parameters are based on experimental conditions obtained in HWT-8[17] and are detailed in Table 3 below.

Table 3: Simulation conditions used for initial roughness design

Parameter	Value	Unit
M_∞	8.0	-
ρ_∞	0.024803	kg/m^3
p_∞	330.743	Pa
T_∞	44.9	K
T_0	620.0	K
T_w	279.0	K
Re_∞/l	9584257	m^{-1}
r_n	0.5	mm

From these parameters, a converged smooth cone meanflow is computed. Figure 4 contains the pressure contour of the meanflow simulation. Since the simulation is axisymmetric, a single slice of the physical domain is depicted. The domain is bounded at the top by the bow shock and below by the cone surface.

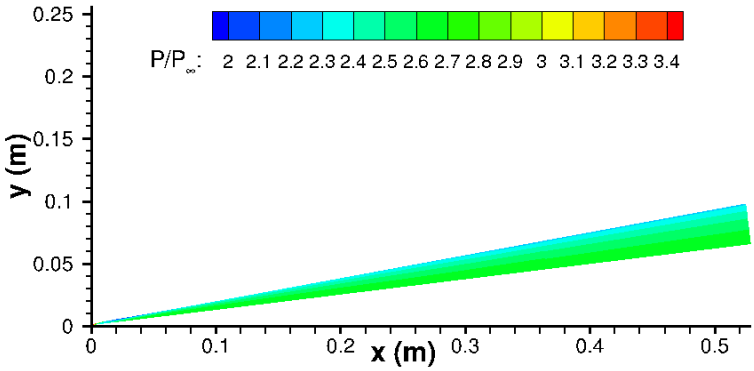

Figure 4: Pressure contour over cone frustum ($M_\infty = 8.0,\ r_n = 0.5\ mm$).

B. Stability Analysis

From the meanflow data, a N-factor plot for Mack's 2nd mode is computed. Using the empirical e^N method, disturbances in the boundary layer are measured by integrating the amplitude growth at a fixed frequency as the disturbance propagates downstream. The amplitude growth is found from LST using a steady parallel flow boundary layer profile obtained from the meanflow data. The N-factor plot in Fig. 5 below contains a frequency range from 180 to 400 kHz. Based on a previous experiment by Casper et. al.,[17] the intermittent turbulence results for the same cone geometry with the same Mach number and similar unit Reynolds number indicated that at 0.34 m, the instability wave intermittency began to drop as turbulent intermittency picked up. Comparing this location on Fig. 5, the location corresponds to an N-factor of 5.19 for a frequency of 240 kHz. Taking 240 kHz as the mode S frequency most likely to start turbulent transition, it can be targeted and damped using transition-delay roughness strips.

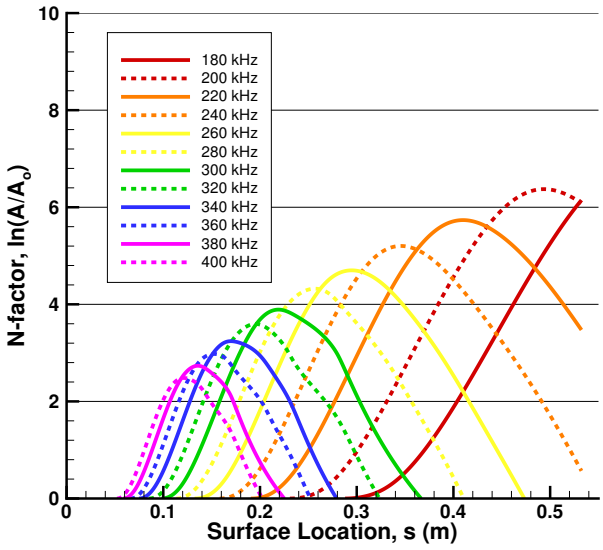

Figure 5: N-factor of mode S growth rate.

The phase speed and growth rate plot for the target frequency is given in Fig. 6 below. The complete mode F plot could not be obtained directly from LST, thus the synchronization location was obtained by connecting the ends of mode F and noting where it crosses mode S. A synchronization location of $s = 0.2436\ m$ along the cone surface was determined. A single axisymmetric roughness strip implemented at this location

will dampen the 240 kHz disturbance per the patented process. The implementation of roughness strips downstream of this first strip will act to suppress unstable frequencies lower than 240 kHz.

The growth rate for mode F and mode S at the target frequency is also determined. Figure 6 shows that mode S becomes unstable at $s = 0.1589\ m$ ($RF = 0.1737$) and becomes stable again at $s = 0.3452\ m$ ($RF = 0.2566$), meanwhile mode F remains entirely stable at the target frequency. Moreover the synchronization location of $s = 0.2436\ m$ ($RF = 0.2114$), whether coincidentally from interpolation, nominally corresponds to the peak growth rate of mode S.

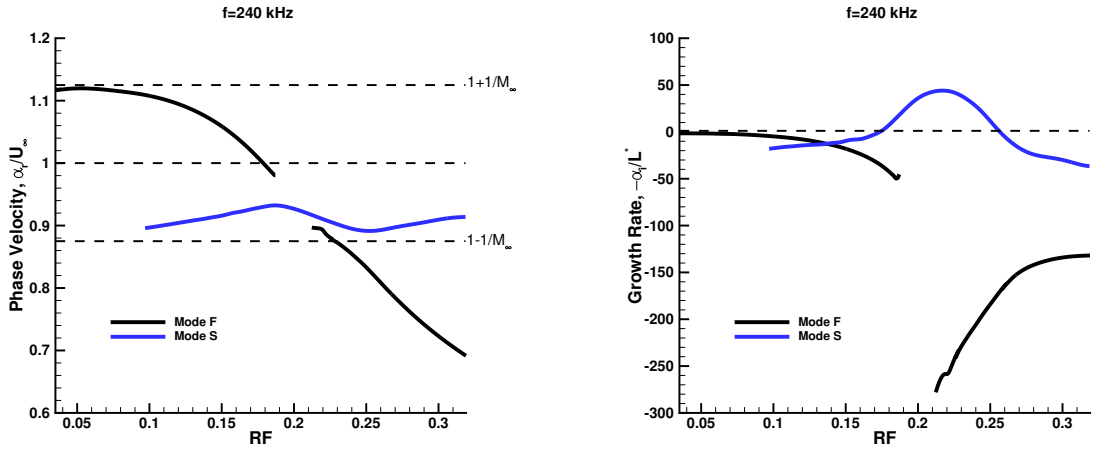

(a) (b)

Figure 6: (a) Phase velocity and (b) growth rate for mode F and mode S at 240 kHz.

C. Design Details

Moving on to the physical design of the transition-delay roughness strip; the location, height, and width of the element must be determined. In a previous computational/experimental collaboration that implemented the same design process, Fong et. al.[11] used elements that were half the local boundary layer thickness in height and twice the boundary layer thickness in width; these same ratios are used here. Furthermore, following a convention set by Fong et. al.[11] in order to guarantee the suppression of the target frequency , the surface location of the element is placed 5 cm downstream of the synchronization location at $s = 0.2936\ m$. Figure 7 contains the boundary layer profile at $s = 0.2936\ m$; the δ_{99} measure of the profile is used as the boundary layer thickness. Table 4 contains the roughness element parameters at the first location.

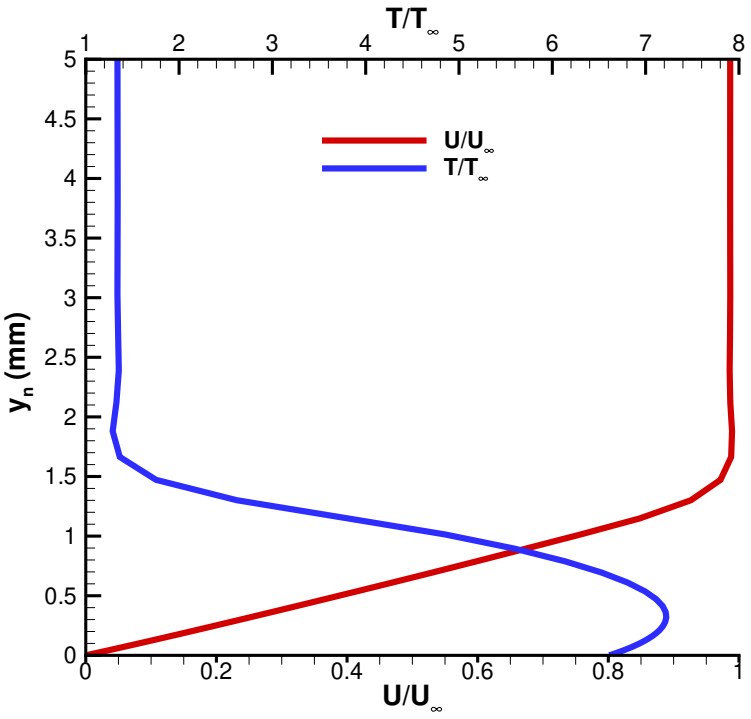

Figure 7: Velocity and thermal boundary-layer height at the first roughness location, $s = 0.2936\ m$

Table 4: Roughness parameters for first roughness element in array

Parameter	Value	Unit
s	0.2936	m
δ_{99}	1.627	mm
h	0.8135	mm
w	3.254	mm

In order to suppress Mack's 2nd mode instability over a wider frequency range, multiple strips are placed downstream of the first roughness strip location. The downstream spacing of the strips is measured as twenty times the boundary layer thickness of the previous strip location. Since the boundary layer thickness increases downstream, the physical dimensions of each roughness strip changes but the proportions are kept the same as described above. The dimensions for the complete roughness-array designed for the simulated cone described in Table 3 is given in Table 5. Note that the locations of the arrays are calculated based on the surface length, s. For convenience, the x-direction locations for each array is also given, where x=0 is measured from the tip of a corresponding sharp cone with the same half-angle.

Table 5: Roughness element details as designed

Strip	Surface, s (m)	x-location, x (m)	Height, h (mm)	Width, w (mm)
1	0.2936	0.2943	0.813	3.254
2	0.3261	0.3265	0.864	3.457
3	0.3607	0.3609	0.916	3.663
4	0.3973	0.3972	0.955	3.819
5	0.4355	0.4351	1.001	4.006
6	0.4756	0.4749	1.053	4.211

In the implementation of the design however some of the dimensions listed in Table 5 need to be simplified for manufacturing purposes. The roughness strips are produced by adhering thermal tape to the test article. The tape has a nominal height of 0.2 mm with taller heights approximated by stacking the tape. Thus, the dimensions of the roughness as implemented in the Mach 8 are given in Table 6. The same roughness strip configuration was also tested in the Mach 5, however, the trip height and width was scaled down by 80% to account for the thinner boundary layer.

Table 6: Roughness element details as implemented experimentally at Mach 7.84

Strip	Surface, s (m)	x-location, x (m)	Height, h (mm)	Width, w (mm)
1	0.2936	0.2943	0.8	3.2
2	0.3261	0.3265	0.8	3.2
3	0.3607	0.3609	0.8	3.2
4	0.3973	0.3972	1.0	4.0
5	0.4355	0.4351	1.0	4.0
6	0.4756	0.4749	1.0	4.0

V. Results

A. Mach 8 Computational and Experimental Results

1. Computational Results

Every simulation of the roughness-suppression effect starts with the simulation of the smooth surface geometry in order to provide a no-roughness meanflow for reference. The stability analysis of the no-roughness meanflow provides the data necessary for designing a transition-delaying roughness array. Moreover, an unsteady simulation of the no-roughness case is used to evaluate the design's effectiveness in suppressing Mack's 2nd mode instability. Figure 8 contains the pressure and temperature contour plots of the Mach 8 case with a nose radius of 0.05 mm. Both contour plots are typical for blunt cones with a very small nose radius. The pressure contours show a moderate pressure increase from the freestream pressure across the shock as well as a favorable pressure gradient moving downstream on the cone's surface. The temperature contours also show a steep thermal gradient limited to the boundary layer. It is from this meanflow that the boundary layer profiles needed for linear stability analysis are obtained.

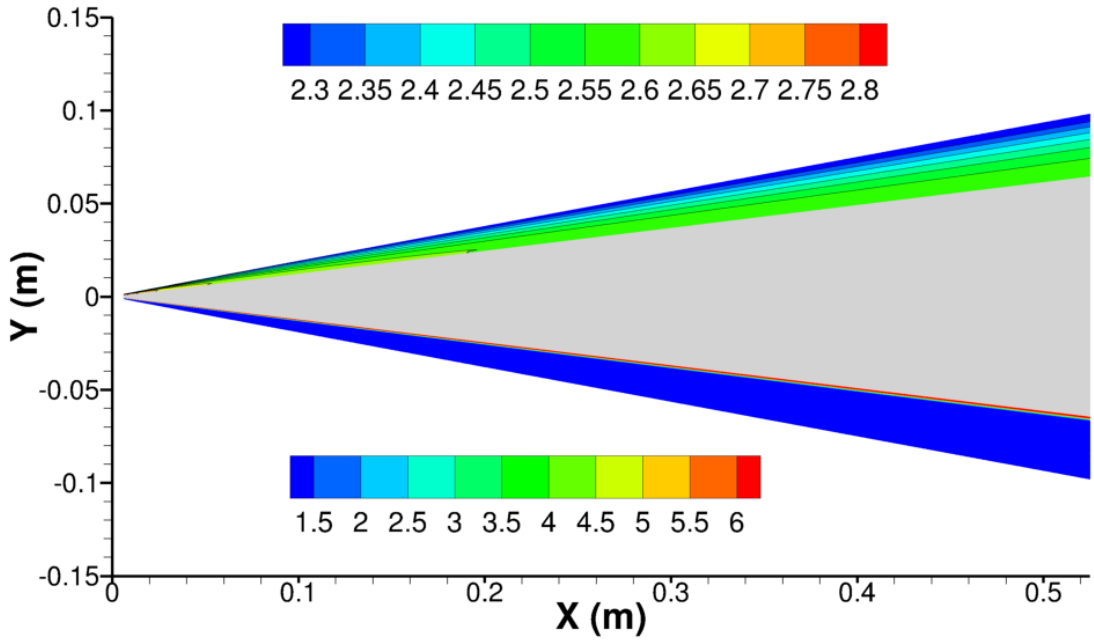

Figure 8: Meanflow pressure ratio P/P_∞ (top) and temperature ratio T/T_∞ (bottom) contours over smooth cone.

Typically, the first step in designing a transition-delaying roughness array is to identify the frequency most likely to start transition. Since the roughness array in this simulation was designed for a cone with a nose radius of 0.5 mm (and a freestream Mach number of 8.0) and carried out on a test article with a nose radius of 0.05 mm (and $M_\infty = 7.84$) it is important to identify which frequencies are being targeted by the roughness array. Therefore, this simulation, with $r_n = 0.05$ mm and $M_\infty = 7.84$ was performed to obtain a direct comparison between experiment and simulation.

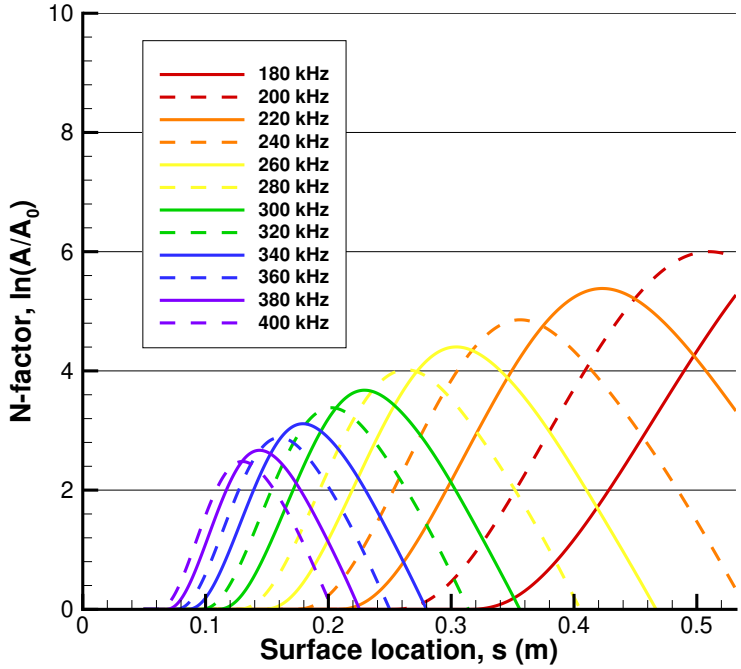

Figure 9: N-factor of Mack's 2nd mode growth rate.

In Casper et al.,[17] the $r_n = 0.5\ mm$ blunt cone was known from experiment to undergo intermittent turbulence at $\approx 0.34\ m$. In Haley and Zhong,[12] which details the design of the roughness, the N-factor analysis of the $r_n = 0.5\ mm$ blunt cone showed that the intermittent turbulence location corresponded with an instability frequency of 240 kHz. For the $r_n = 0.05\ mm$ simulation currently in question the same location corresponds to a peak instability frequency of approximately 260 kHz as seen in Fig. 9 (on this sharper cone, the onset of turbulence is slightly upstream of the 0.34 m location).

This 260 kHz frequency however is not the cut-off frequency of the roughness-array, for which frequencies higher than 260 kHz are suppressed by the leading roughness strip. This frequency is instead 228 kHz, which is determined by identifying the frequency of the so-called synchronization point (where mode F and mode S become weakly coupled) corresponding to the array at $s = 0.2936\ m$. Figure 10 plots the phase speed and growth rate at 228 kHz. Due to the coupling between Mode S and mode F and the branch cut between mode F^+ and mode F^- it is difficult to resolve a complete phase speed plot (this difficulty also appears to be aggravated by conical flow fields). The so-called synchronization point as described by Fong et al.[10] was determined by connecting the ends of mode F^+ and mode F^- as illustrated by the red dashed line in Fig. 10a and noting where it intersects with mode S. For 228 kHz this intersection occurs at $s = 0.2936\ m$, thus for a single roughness strip at this location, frequencies higher than 228 kHz are predicted to be suppressed while lower frequencies are predicted to be amplified. The purpose of the additional downstream roughness strips is to suppress these amplified lower frequencies.

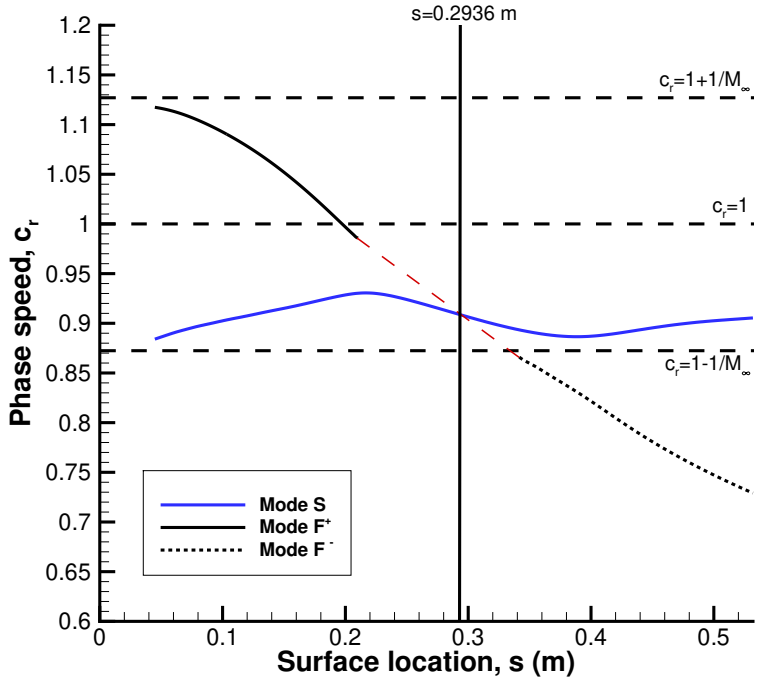

(a)

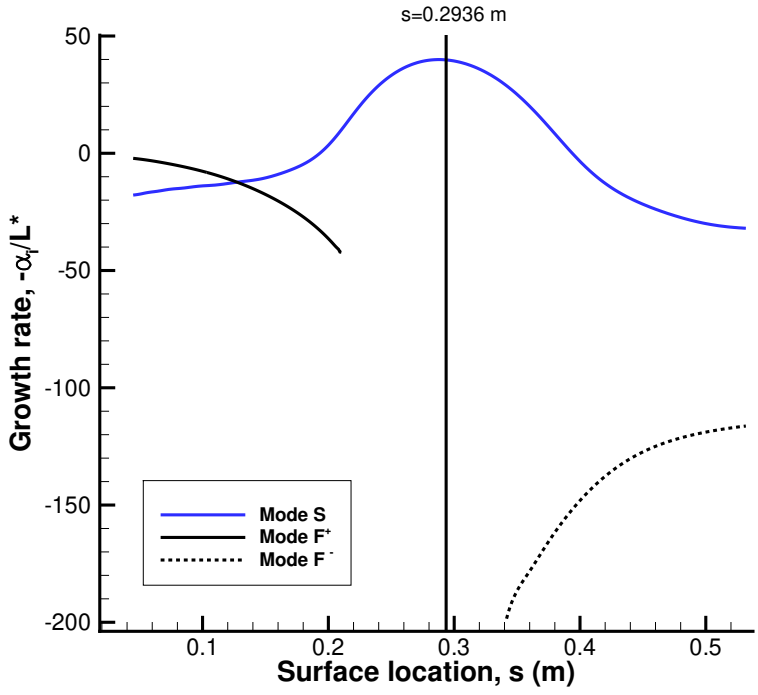

(b)

Figure 10: (a) Phase speed and (b) growth rate for mode F and mode S at 228 kHz.

In theory,[18] since mode S and mode F are not synchronized at a single wave number α and angular frequency ω, but instead are weakly coupled over a range of wave numbers for a given frequency it is important to note how our intersection approximation for phase speed relates to the growth rate in Fig. 10b. Looking at Fig. 10b, the roughness nominally corresponds to the peak unsteady growth rate for mode S also known as Mack's 2nd mode instability. Whether this is significant or just a coincidence of the intersection approximation is not clear.

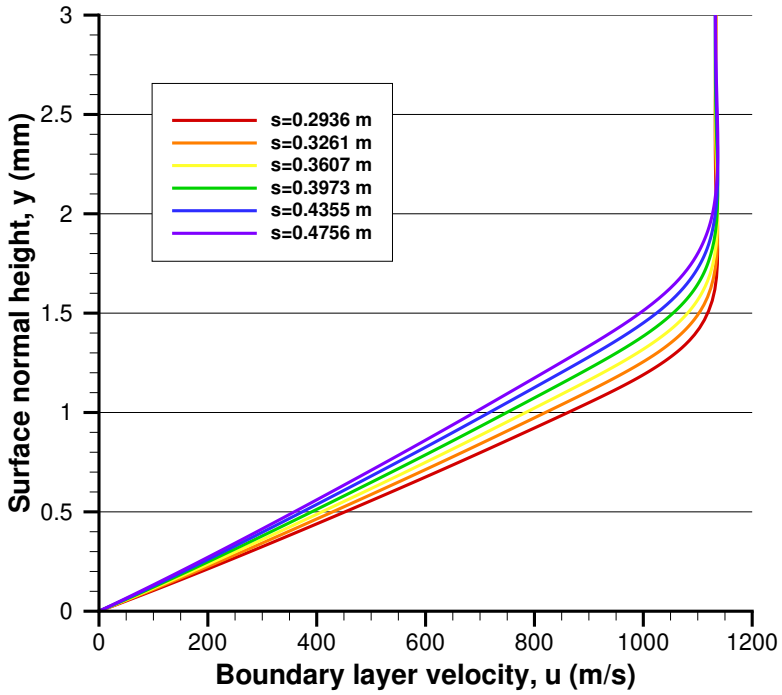

Figure 11: Boundary layer profile at each of the roughness locations.

Figure 11 provides the smooth cone boundary layer profiles at each of the six roughness locations. As designed for a 0.5 mm nose radius blunt cone, the strips where designed to be half the boundary-layer thickness in height and twice its thickness in width. Since the current simulation and experiment is for a sharper 0.05 mm nose radius, it is important to know if any difference in the boundary layer thickness have significantly changed the ratio of the roughness height to the boundary layer thickness. Table 7 shows that the changes are minimal. So long as the roughnesses are submerged within the boundary layer they should be capable of suppressing Mack's 2nd mode instability.[10]

Table 7: Ratio of roughness heights to boundary layer thickness for Mach 8 case

Surface, s (m)	BL Height (mm)	Sim. Height (mm)	Ratio	Exp. Height (mm)	Ratio
0.2936	1.649	0.813	0.493	0.8	0.485
0.3261	1.738	0.864	0.497	0.8	0.460
0.3607	1.828	0.916	0.501	0.8	0.438
0.3973	1.918	0.955	0.498	1.0	0.521
0.4355	2.051	1.001	0.488	1.0	0.488
0.4756	2.067	1.053	0.509	1.0	0.484

Now that it has been established that the roughness-array is adequately designed to suppress Mack's 2nd mode within the context of the smooth meanflow and linear stability theory, the meanflow with the roughness-

array can be simulated. The pressure and temperature contours for the cone with surface roughness are featured in Fig. 12. Figure 12a shows that the Mach waves produced by the leading edge of each roughness strip merge within the shock layer. From the pressure contours it would appear that these merged Mach wave will not reach the shock boundary. This is contrasted with a single roughness strip that will produce a distinct Mach wave whose angle will intersect with the shock boundary.[12] The temperature contours in Fig. 12b show a significant increase in temperature ratio over the smooth cone simulation in Fig. 8. The increased temperature ratio is highly localized to the upstream corner of each roughness strip. This indicates that, while the purpose of the roughness array is to delay transition and thus reduce the heat flux to the surface due to turbulence, the strips themselves are subject to increased localized heating. Moreover, the presence of the roughness has caused the thermal boundary layer to thicken and thus the thermal gradient is more visible within the shock layer.

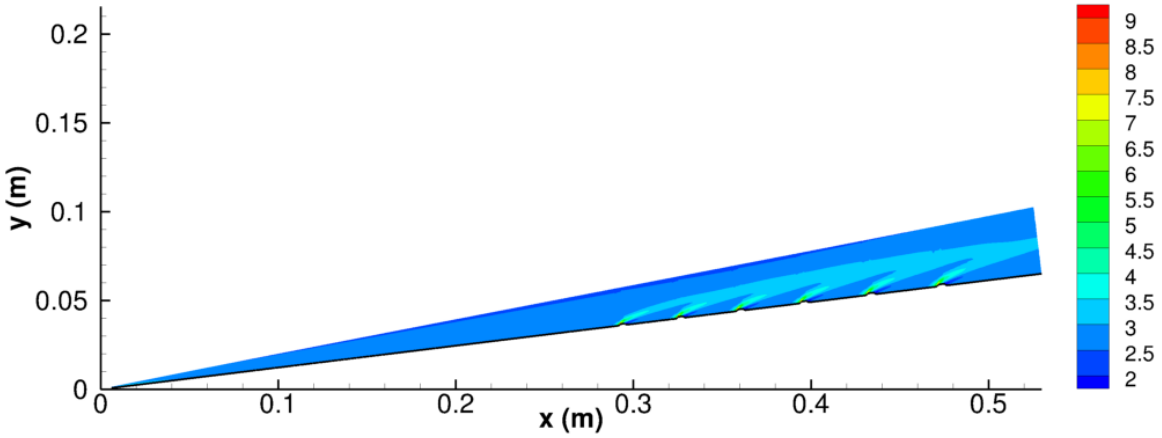

(a)

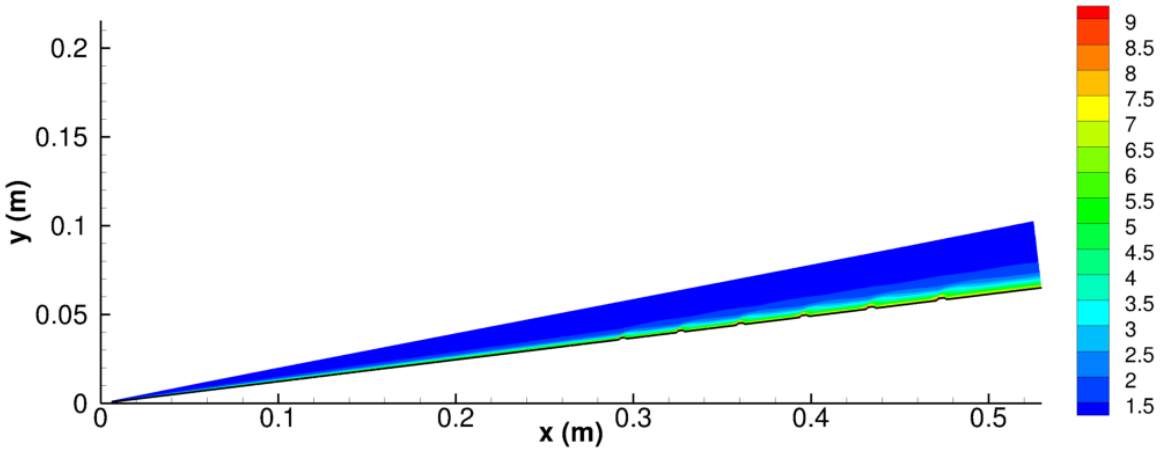

(b)

Figure 12: Meanflow (a) P/P_∞ and (b) T/T_∞ contours over roughness.

A closer look at the pressure field around several of the roughness strips in Fig. 13 show that while the compression region on the leading edge of the roughness is significantly higher than its surroundings it too is fairly localized. The same is also true of the expansion area behind the roughness. It is suspected that the reason for this localization is due to the roughness strips being in an array. By contrast on a single isolated roughness strip these compression and expansion regions lend themselves to creating a clearly defined Mach wave and expansion fan that extends downstream and into the shock layer.[12]

Moreover the streamtraces in Fig. 13 evince a flowfield in which the streamtraces are influenced greatly by

the presence of the roughness strips. Wherein the streamtraces are pushed away from the cone surface. All the while, streamtraces closer to the shock boundary are unperturbed, as would be expected in a supersonic flow. One feature that is missing from the flow are the separation regions on either side of the roughness strip. These regions are present for an isolated roughness on a cone with the same height, width and smooth edges the first strip in the array,[12] and on a flat plate with a half-ellipse roughness.[9] The reason for the separation regions absence here is unclear, however, it may be related to how localized the compression and expansion regions are to the roughness.

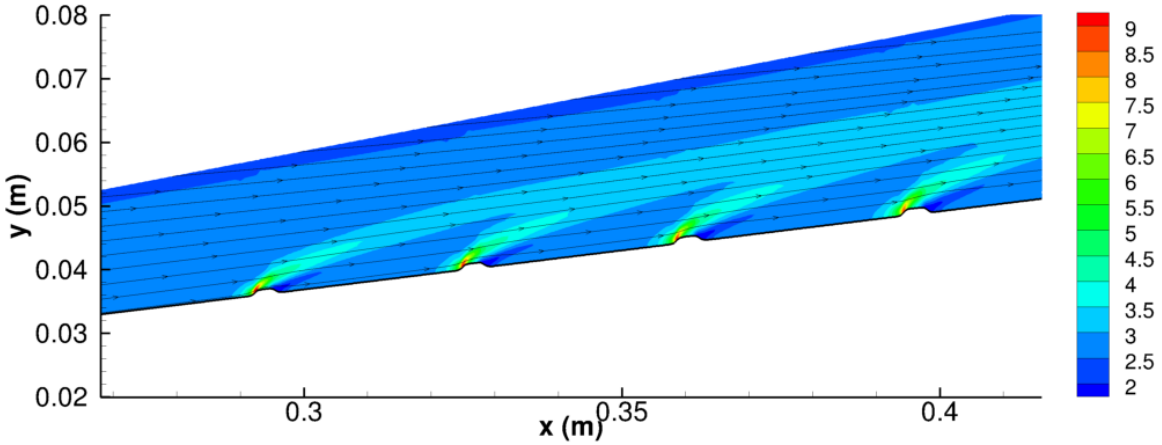

(a) Streamtraces over the four leading elements.

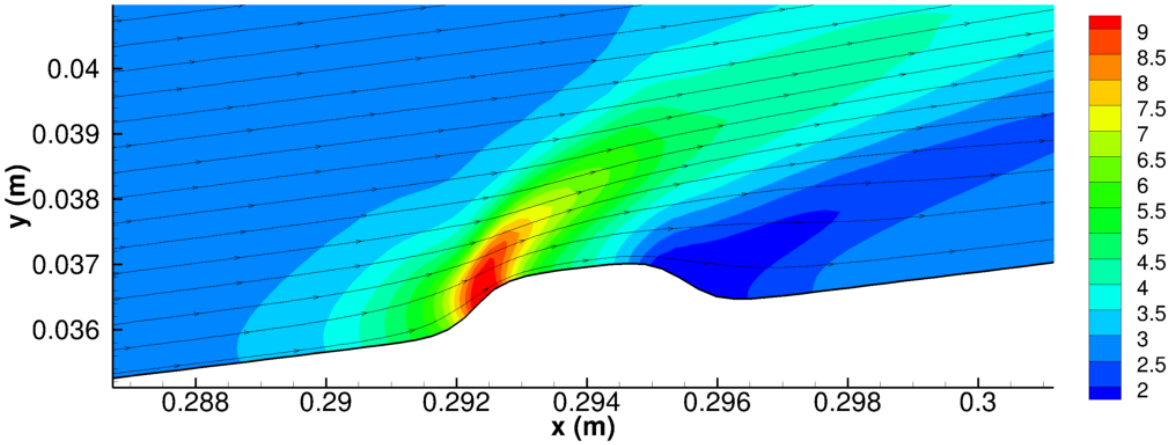

(b) Streamtraces over the first roughness element in the array.

Figure 13: Streamtraces over roughness array and roughness elements over P/P_∞ contour.

Future work for this simulation includes an unsteady simulation of a broadband pulse over the roughness array. FFT analysis of this unsteady simulation will reveal which frequencies are suppressed by the roughness array and which are amplified and where. This provides the deepest insight into the effectiveness of the roughness array. Moreover, it provides power spectrum density data that can be compared to experimental results.

2. Experimental Results

Mach 8 experimental results show that the roughness strips were successful in delaying transition. Fig. 14 shows a comparison of the pressure spectra with and without the roughness elements at two different freestream conditions. At an Re near $7.0 \times 10^6/m$, large second-mode waves near 200 kHz develop without the presence of roughness. These waves are also clearly visible as rope-like waves in the boundary layer in

schlieren images (Fig. 15a). When the roughness is added, much smaller second-mode waves are measured. Also, because the boundary layer thickens with the presence of roughness, the frequency of the waves shifts to lower frequencies near 120 kHz. The corresponding schlieren image (Fig. 15b) indicates a thicker boundary layer, and very faint rope waves are visible from time to time in the full high-speed movies (not seen in this image).

At a higher freestream Re near $9.0 \times 10^6/m$, transition again seems to be delayed, though the results are less clear because the boundary layer is mostly turbulent at this condition. The pressure spectra without roughness show an intermittently turbulent boundary layer by x = 0.422 m. The remnants of second-mode waves near 200 kHz are seen, but there is also broadband frequency content indicating a predominately turbulent boundary layer. Further downstream at x = 0.497 m, the spectra look mostly turbulent. This turbulence is also observed in the schlieren images (Fig. 15c) without roughness.

With roughness on the cone at this higher Re, the pressure spectra look qualitatively similar. At x= 0.422 m, remnants of second-mode waves can again be seen, but at a lower frequency near 120 kHz. Broadband frequency content is at a lower level than observed with the roughness, suggesting a transition delay. Further downstream at x = 0.497 m, the spectra are fairly broadband, but remnants of the waves still exist (while without roughness the spectra appeared fully turbulent). Therefore, qualitatively, the spectra again appear less turbulent. Schlieren images with the roughness (Fig. 15d) also appear less turbulent and in fact the snapshot that is shown indicates the presence of second-mode waves as opposed to a fully turbulent boundary layer as in Fig. 15c.

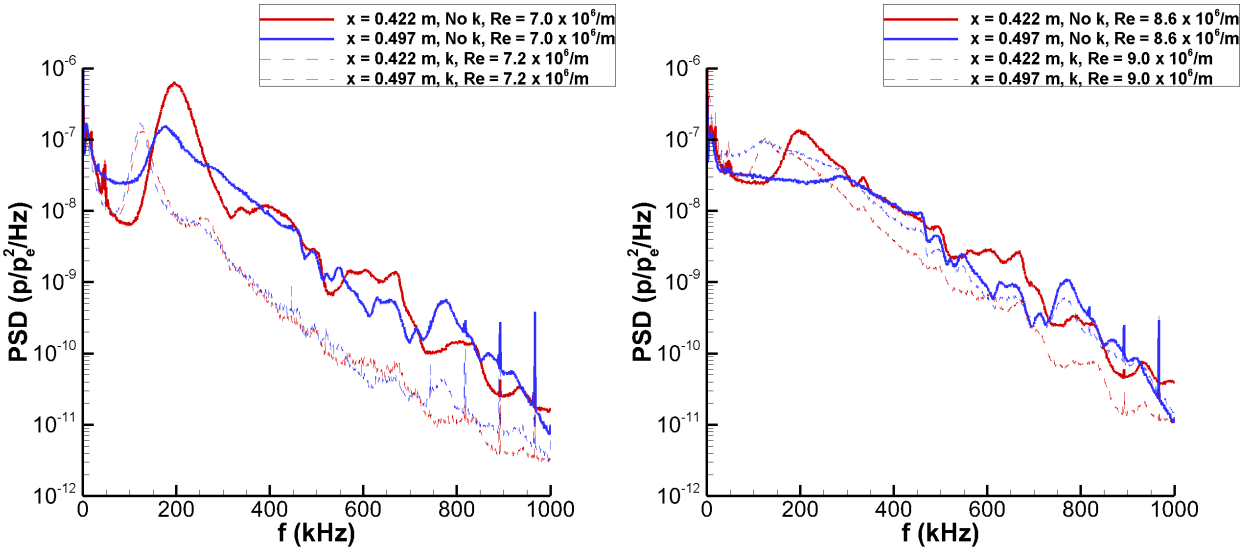

(a) Re near $7.0 \times 10^6/m$.

(b) Re near $9.0 \times 10^6/m$.

Figure 14: Mach 8: comparison of pressure spectra at x = 0.422 and 0.497 m.

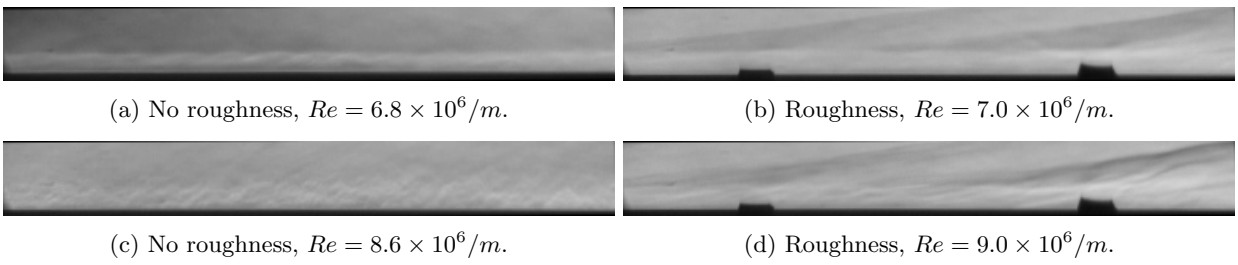

(a) No roughness, $Re = 6.8 \times 10^6/m$.

(b) Roughness, $Re = 7.0 \times 10^6/m$.

(c) No roughness, $Re = 8.6 \times 10^6/m$.

(d) Roughness, $Re = 9.0 \times 10^6/m$.

Figure 15: Mach 8: Schlieren images of the cone boundary layer between x = 0.422 and 0.497 m.

B. Mach 5 Computational and Experimental Results

1. *Computational Results*

A question that has not yet been addressed by the development of Zhong and Fong's laminar flow control strategy is what happens when a transition-delaying roughness array is subjected to off-design flow conditions. In the Mach 8 case there is small change in cone geometry between the roughness' design and its implementation but the flow conditions are nominally the same. In this section the roughness array is applied to a Mach 5 flowfield. The same number of roughness strips with the same downstream spacing is applied to the cone, but the roughness heights and widths are reduced to 80% to keep the roughness immersed within the boundary layer in order that it may suppress the 2nd mode instability. The cone, which is still a 7° half-angle straight cone has a 0.5 mm nose radius like the original Mach 8 design. This Mach 5 case presents an interesting challenge to transition-delaying roughness, as Mach 5 flows are still dominated by 1st mode instabilities, and it is not known if the 1st mode will respond to the roughness strips in the same way as the 2nd mode.

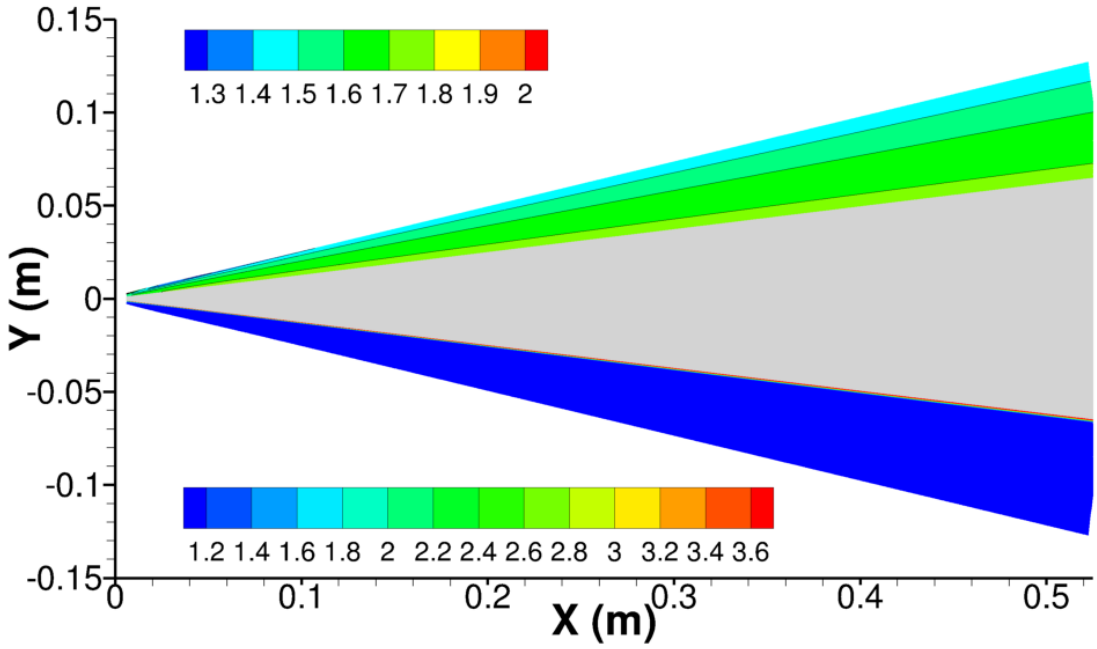

Figure 16: Meanflow pressure, P/P_∞, (top) and temperature, T/T_∞, (bottom) contours over Mach 5 smooth cone.

The first figures for this case are the smooth cone pressure and temperature contours in Fig. 16. Both contours are typical of blunt cone results. There is a moderate pressure increase across the shock and a favorable pressure gradient along the surface. The thermal boundary layer is also tightly confined to the wall.

Wall-normal slices are taken from this simulation and used to compute the N-factors for the meanflow. Figure 17 plots the N-factor results as computed from the 2nd mode over a frequency range of 250 to 700 kHz. As before the first roughness strip is placed at $s = 0.2936$ m which corresponds to an N-value of approximately 1.8 at ≈ 362 kHz; much lower than any N-value though to cause transition. It is unlikely that transition at these flow conditions is due to the 2nd mode instability and is more likely due to the 1st mode instability.

The neutral curve in Fig. 18a shows that the 2nd mode's unstable region is fairly narrow and unlikely to grow significantly. Figure 18b is constructed similarly to the neutral curve but maps the growth rate. Just below the 2nd mode neutral curve we can see the presence of the stable 1st mode. The 1st mode is stable in the figure because the plot was computed for a 2-D planar wave; the 1st mode is most unstable when considering oblique waves. A complete stability analysis which thoroughly investigates oblique waves is an

area for future work.

The synchronization frequency for the first roughness location is identified as 339 kHz; the phase speed and growth rate are plotted in Fig. 19 unlike the plots of phase speed and growth rate previously presented, these plots show a different mode coupling behavior, which consequently makes it difficult to determine their synchronization location. The coupling behavior shows that mode S does not stay bounded between $c_r = 1 - 1/M_\infty$ and $c_r = 1$, but instead appears to follow the route typically taken by mode F. Fedorov and Tumin explain this is due to the location of the branch points in the α-plane which can move about the plane with slight variations in flow parameters between flowfields.[18] As such, it is difficult to determine where the so-called synchronization location is as currently defined by Zhong and Fong's laminar control strategy as the intersection of mode S and mode F. Instead, in this paper we take the peak unsteady growth rate at $s = 0.2936\ m$ to determine the synchronization frequency of 339 kHz.

Whether the roughness array will suppress any frequencies above 339 kHz is suspect. This is because the 2nd mode instability is already pretty weak and the effect of the 1st mode is not accounted for by the passive laminar control strategy.

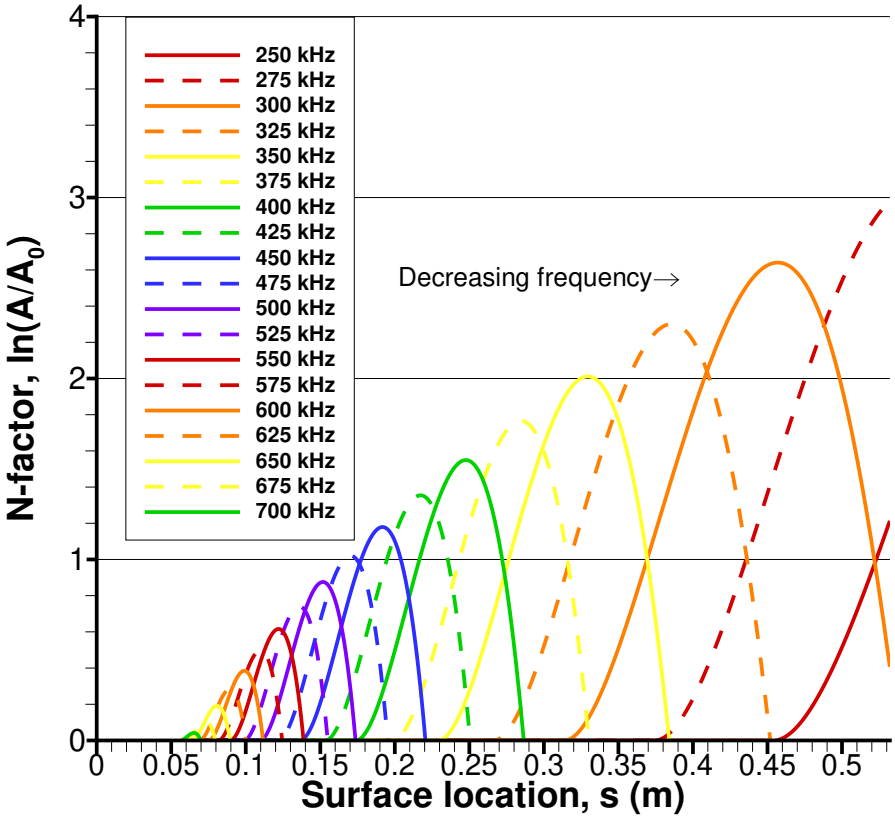

Figure 17: N-factor of Mack's 2nd mode.

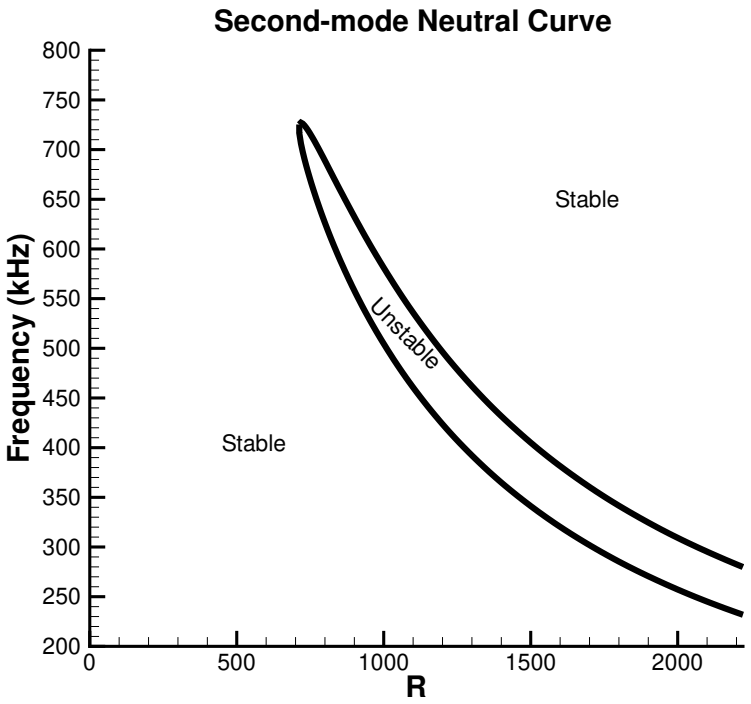

(a)

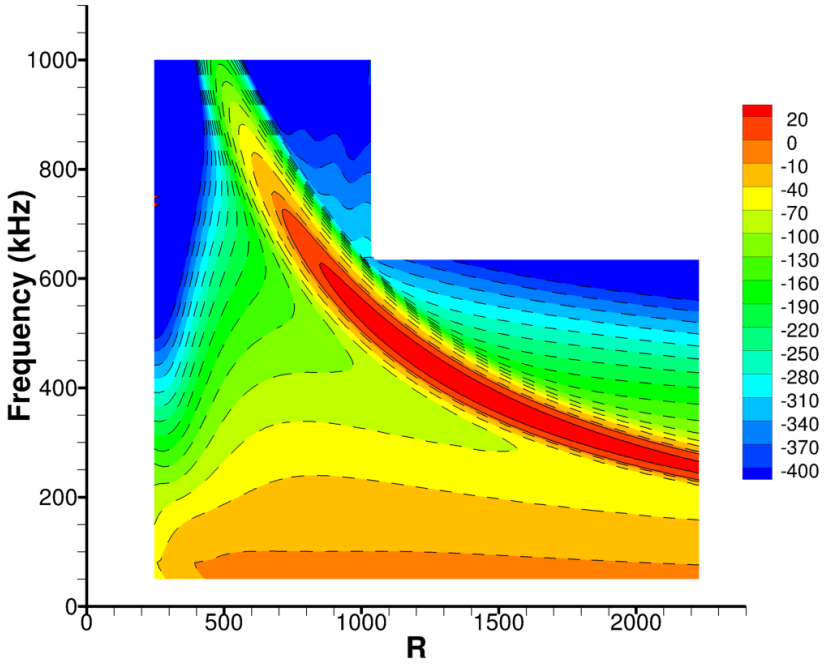

(b)

Figure 18: (a) Neutral curve of Mack's 2nd mode for a 2-D wave. (b) Growth rate map (α_i/L^*) of mode S for a 2-D wave.

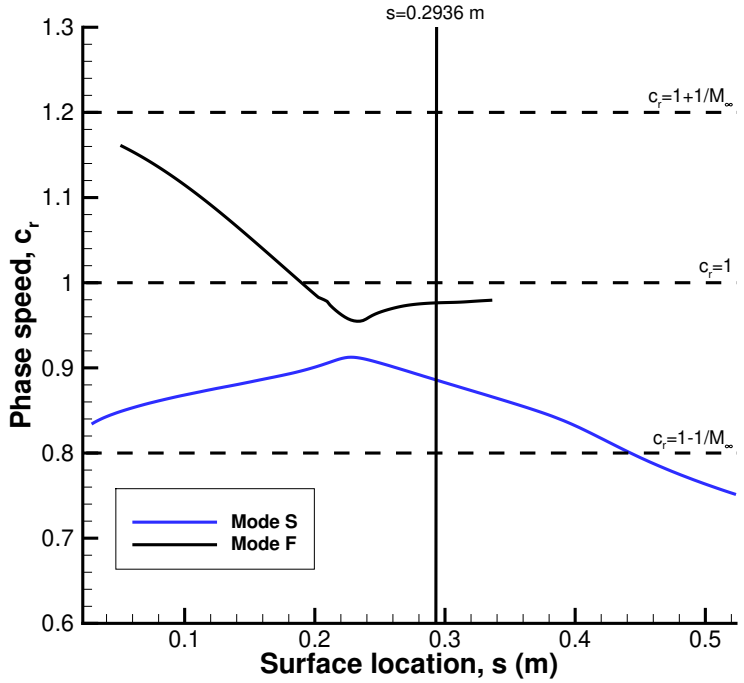

(a)

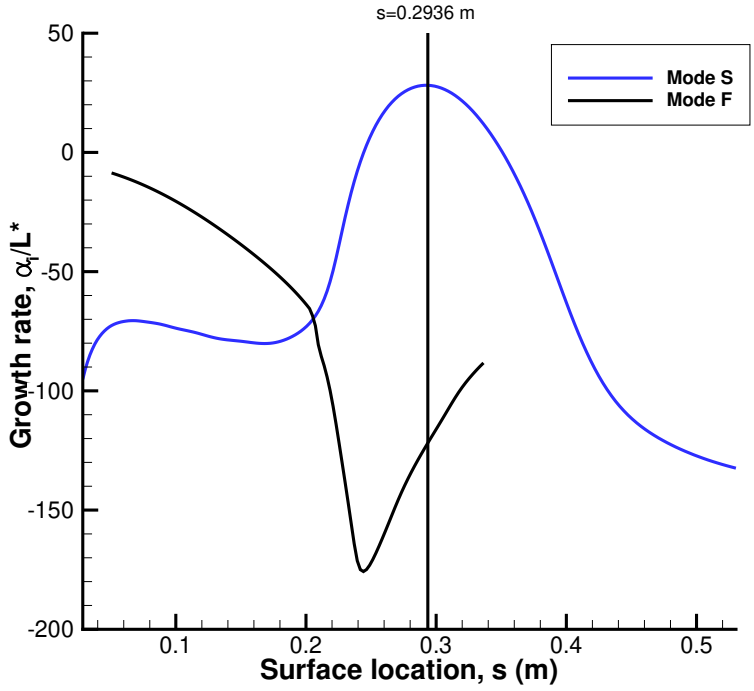

(b)

Figure 19: (a) Phase velocity and (b) growth rate for mode F and mode S at 339 kHz.

In order to give the roughness array a fighting chance, however, the roughness height and width was reduced to keep in immersed within the boundary layer. Since the boundary layer thickness is proportional to the square root of the boundary layer thickness, the roughness heights and widths were rescaled by $\sqrt{M_5/M_8} \approx 80\%$. Figure 20 plots the boundary layer thickness at each of the roughness locations. Table 8 shows that the rescaling was able to maintain a ratio of boundary layer thickness to roughness height of approximately 1:2.

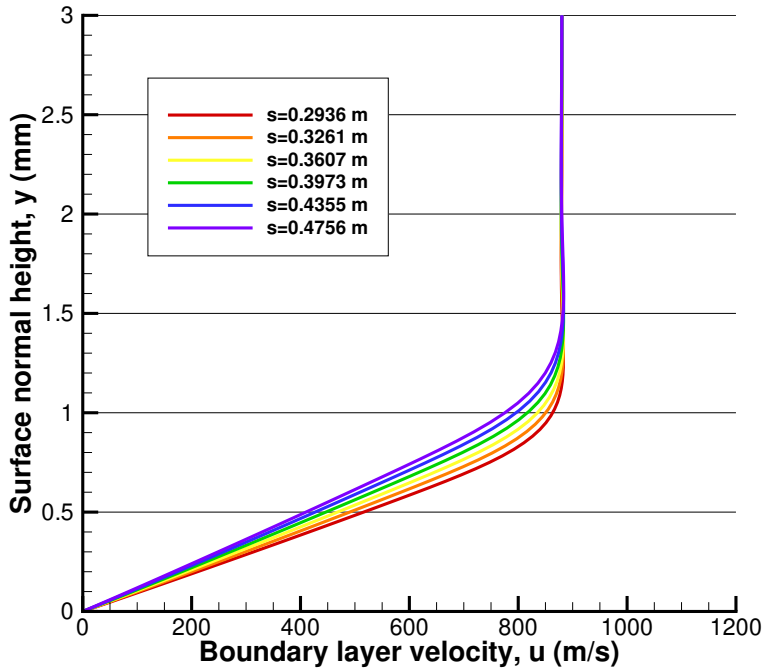

Figure 20: Boundary layer profile at each of the roughness locations.

Table 8: Ratio of roughness heights to boundary layer thickness for Mach 5 case

Surface, s (m)	BL Height (mm)	Sim. Height (mm)	Ratio	Exp. Height (mm)	Ratio
0.2936	1.120	0.650	0.580	0.6	0.536
0.3261	1.262	0.691	0.548	0.6	0.475
0.3607	1.321	0.733	0.555	0.6	0.454
0.3973	1.387	0.764	0.551	0.8	0.577
0.4355	1.448	0.801	0.553	0.8	0.538
0.4756	1.511	0.842	0.557	0.8	0.529

The pressure and temperature contours for the cone with surface roughness are presented in Fig. 21. Figure 21a shows that the Mach waves produced by the leading edge of each roughness strip are very weak and are difficult to distinguish from the shock layer. The temperature contours in Fig. 21b show a moderate increase in the temperature ratio over the smooth cone simulation in Fig. 16. And just like the Mach 8 case, the presence of the roughness has caused the thermal boundary layer to thicken and thus the thermal gradient is more visible within the shock layer. All together, the roughness does not appear to have a significant influence over the meanflow.

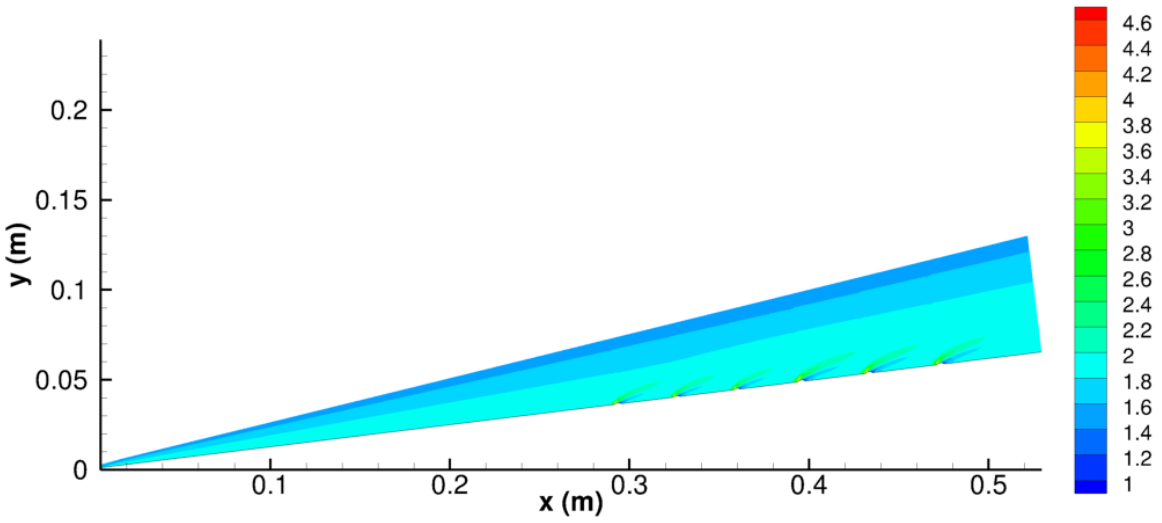

(a)

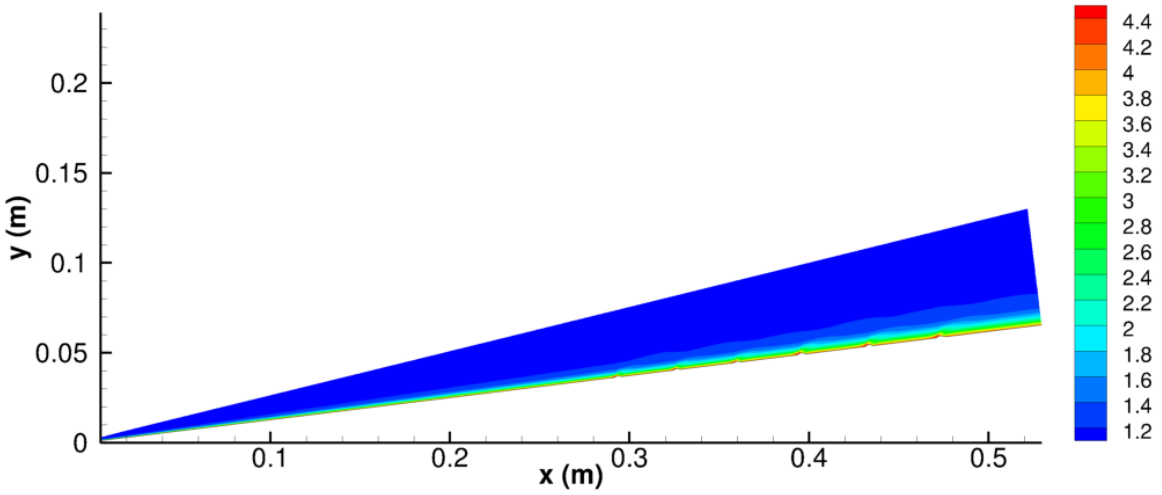

(b)

Figure 21: (a) Meanflow pressure, P/P_∞ , and (b) temperature, T/T_∞, contours over roughness array.

A closer look at the pressure field around several of the roughness strips in Fig. 22 show that the compression and expansion regions are fairly localized just like the Mach 8 simulation. This may be do to the fact that the roughnesses are in an array, as is suspected for the Mach 8 case, but may also be because the Mach number is lower and resulting Mach waves and expansion fans off of the strip are reduced in strength.

The streamtraces in Fig. 22 show that the boundary layer thickness is influenced by the presence of the roughness strips causing it to grow. This is evidenced by the closest wall streamtrace being nudged further from the wall every time is interacts with a roughness strip. And lastly, one feature that is missing again are the separation regions on either side of the roughness strip. The reason for their absence here is unclear, however, it may be related to how localized the compression and expansion regions are to the roughness.

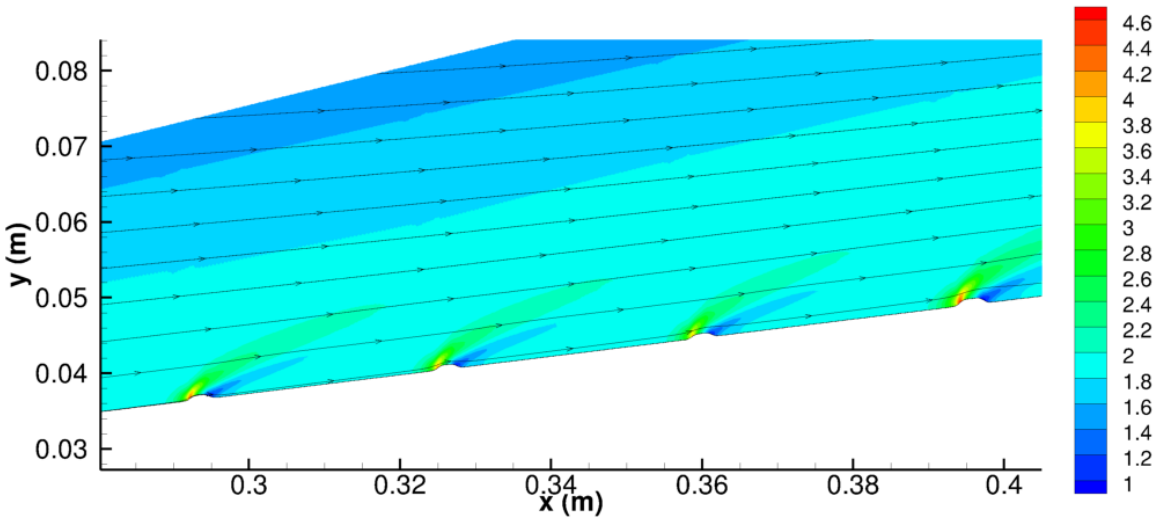

(a)

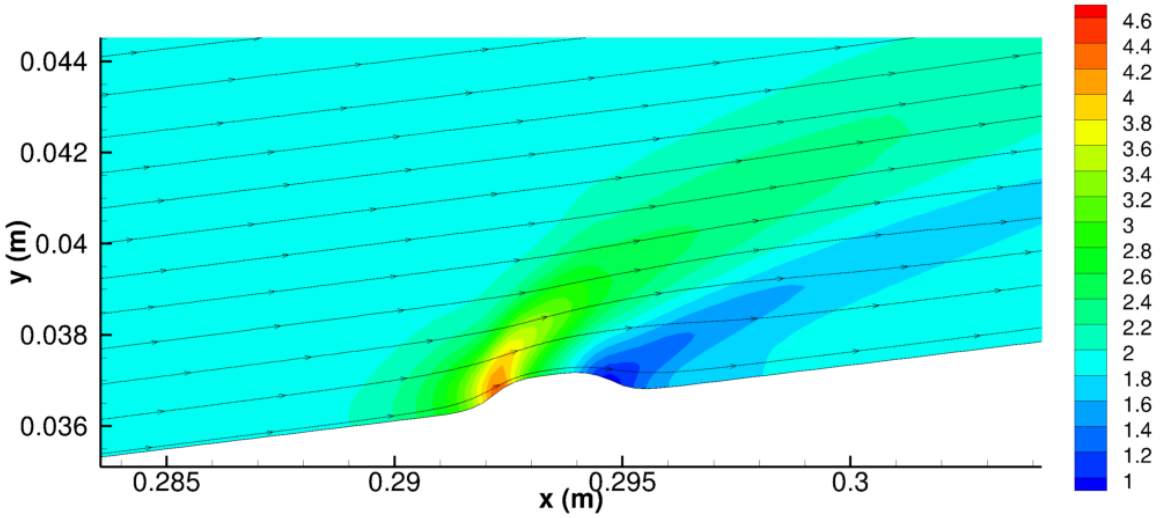

(b)

Figure 22: (a) Meanflow pressure contours, P/P_∞ ,over roughness. (b) Stream trace around roughness element.

Future work for this simulation includes doing a thorough analysis of the the 1st mode instability using LST, as well as an unsteady simulation of a broadband pulse over the roughness array. As mentioned previously, FFT analysis of the unsteady data will reveal which frequencies are suppressed by the roughness array and which are amplified and where.

2. Experimental Results

Unfortunately, experimental results at Mach 5 indicated that the roughness strips did not delay transition. This result is likely because at Mach 5, both first and second-mode waves show significant growth.[17] Therefore, the delay mechanism used at Mach 8 to delay second-mode transition may in fact promote the growth of first-mode waves at Mach 5.

Figure 23 shows a comparison of the pressure spectra measured with and without the roughness elements. Without roughness, large second-mode waves are observed near 250 kHz at x = 0.422 m. The boundary layer also appears intermittently turbulent, as indicated by the rise of broadband frequency content. Further

downstream at x = 0.497 m, the boundary layer has transitioned to turbulence. With roughness, the boundary layer is already turbulent by x = 0.422 m. Further downstream, broadband turbulence is still observed, but with an additional peak near 100 kHz. These may be additional disturbances introduced by the presence of the roughness.

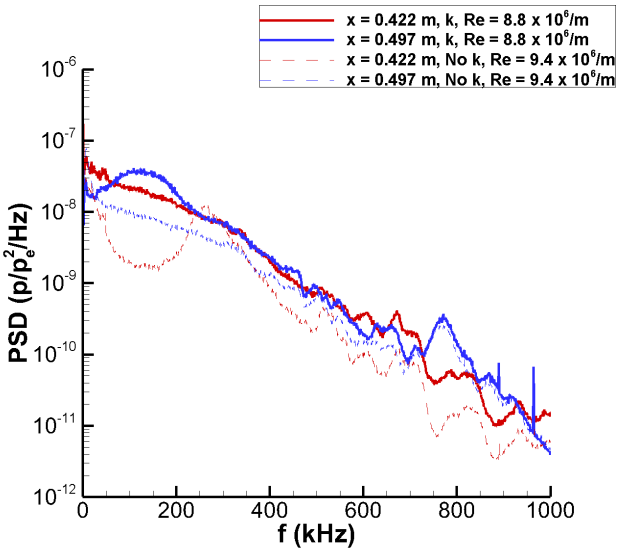

(a) Re near $9.0 \times 10^6/m$.

Figure 23: Mach 5: comparison of pressure spectra at x = 0.422 and 0.497 m.

Schlieren movies both with and without the roughness verify the pressure spectra results. Figure 24a shows the boundary layer without roughness. At the front of the image, the boundary layer is mostly laminar with a second mode instability wave packet. By the end of the image, the boundary layer is turbulent. The full movie shows that the boundary layer at the front of the cone is intermittently turbulent, while it remains fully turbulent downstream. The presence of roughness (Figure 24b) modifies the boundary layer and makes it thicker, however the boundary layer continues to appear turbulent throughout the entire movie, again indicating no delay of transition with roughness strips at Mach 5.

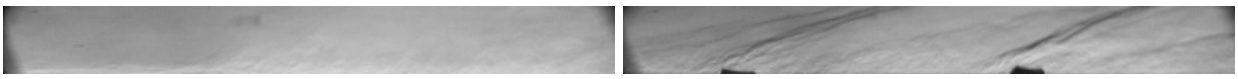

(a) No roughness, $Re = 9.4 \times 10^6/m$.

(b) Roughness, $Re = 8.8 \times 10^6/m$.

Figure 24: Mach 5: Schlieren images of the cone boundary layer between x = 0.422 and 0.497 m.

VI. Conclusion

This joint numerical and experimental investigation of the roughness-suppression effect has three main takeaways. The first is that a roughness-array designed to suppress Mack's 2nd mode instability was implemented on a test article and transition was successfully delayed. Not only was transition delayed but PSD results show that the frequencies targeted for suppression were in fact the frequencies suppressed. Not only does this result provide the duly needed additional physical evidence of the suppression phenomenon, it also shows that the phenomenon exists in boundary layers that grow downstream and contain a range of unstable frequencies.

The second important result is that the roughness-arrays are not effective when applied to off-design flow fields. It appears that slight changes in geometry are permissible, such as the nose radius, but significant changes to the flow conditions, such as Mach number, are detrimental. The experimental results show that the roughness-array not only did not delay transition in the Mach 5 case but may have also interacted with

the 1st mode and promoted transition.

This result points to the speculation that roughness-arrays may not be able to suppress 1st mode transition as it does the 2nd mode. A hypothesis would be that the 1st mode cannot be suppressed in the same manner because, although it synchronizes with the slow acoustic, the instability does not arise from mode coupling. To extend this hypothesis further, one could predict that the other Mack mode instabilities (e.g. 3rd, 4th, etc.) can be suppressed because they weakly couple with other fast modes (e.g. F2, F3, etc.).

This talk of weakly coupling modes leads into the last important takeaway from this work, the importance of accurately describing the so-called synchronization location. Three sets of phase speed and growth rate plots have been presented in this paper; each one sightly different from the last. For the Mach 8 cases the synchronization location was determined by interpolation, for the Mach 5 case it was determined from the peak growth rate. As it turned out the interpolated locations for the Mach 8 cases closely corresponded with the peak growth rate too. Since the truth of the matter is that mode F and mode S become coupled and the real part of their wave numbers become close in value (or equal), using a simple mode intersection to determine the synchronization location becomes perilous. Instead the results in the paper would suggest placing the roughness at the peak growth rate of the frequency you want to suppress.

VII. Future Work

The work in this investigation is by no means complete. In regard to the numerical simulation there is additional stability work that can be done such as computing the stability characteristics for oblique waves and investigating Mack's 1st mode instability at Mach 5 as well as quantifying how the meanflow velocity and thermal boundary layers change in the presence of the roughness array. But perhaps the most important work to be done is to compute the unsteady simulations where a broad bandwidth perturbation is introduced to the boundary layer and individual frequencies can be examined for suppression or amplification. The results of an unsteady simulation are more readily compared with the experimental results already presented in the this paper.

A direction for future work is to develop a stability analysis tool that can better resolve the coupling between mode S and mode F on a cone. Whether this development is a correction to current LST tools or is a wholly new analysis tool, such as the multi-mode decomposition of unsteady DNS data, is difficult to say. But what is becoming more apparent is that if this roughness-suppression phenomenon is to be understood correctly it is not sufficient to describe the interaction between mode F and mode S as the synchronization of two modes (where they share a single wavenumber, α, and angular frequency, ω) but more accurately as the weak coupling of the two modes (see Fedorov et al. for theoretical model of weak mode coupling[18]). To not do so only hinders the description of a physical mechanism.

Acknowledgements

This research was supported by the U.S. Air Force Office of Scientific Research, USAF, under AFOSR Grant #FA9550-15-1-0268, monitored by Dr. Ivett Leyva. Primary computational resources were provided by the AFOSR with additional computational resources provided by Extreme Science and Engineering Discovery Environment (XSEDE) through Texas Advanced Computing Center (TACC) and San Diego Supercomputer Center (SDSC) under grant number TG-ASC090076, supported in part by the National Science Foundation. The views and conclusions contained herein are those of the authors and should not be interpreted as necessarily representing the official policies or endorsements, either expressed or implied, of the U.S. Air Force Office of Scientific Research or the U.S. Government.

These experiments greatly benefited from the support of John Henfling, Russell Spillers, and Seth Spitzer, all of Sandia National Laboratories. Sandia National Laboratories is a multi-mission laboratory managed and operated by National Technology and Engineering Solutions of Sandia, LLC., a wholly owned subsidiary of Honeywell International, Inc., for the U.S. Department of Energy's National Nuclear Security Administration under contract DE-NA0003525.

References

[1]Zhong, X. and Wang, X., "Direct Numerical Simulation on the Receptivity, Instability, and Transition of Hypersonic Boundary Layers," *Annual Review of Fluid Mechanics*, Vol. 44, 2012, pp. 527–561.

[2]Fedorov, A., "Transition and Stability of High-Speed Boundary Layers," *Annual Review of Fluid Mechanics*, Vol. 43, 2011, pp. 79–95.

[3]Mack, L. M., "Boundary Layer Linear Stability Theory," Tech. rep., 1984.

[4]Zhong, X., Fong, K. D., and Wang, X., "Hypersonic laminar flow control," 2014.

[5]James, C. S., "Boundary-Layer Transition on Hollow Cylinders in Supersonic Free Flight as Affected by Mach Number and a Screwthread type of Surface Roughness," Tech. rep., 1959.

[6]Holloway, P. F. and Sterrett, J. R., "Effect of Controlled Surface Roughness on Boundary Layer Transition and Heat Transfer at Mach Numbers of 4.8 and 6.0," *Nasa Tn D-2054*, , No. April, 1964.

[7]Fujii, K., "Experiment of the Two-Dimensional Roughness Effect on Hypersonic Boundary-Layer Transition," *Journal of Spacecraft and Rockets*, Vol. 43, No. 4, 2006, pp. 731–738.

[8]Duan, L., Wang, X., and Zhong, X., "A high-order cut-cell method for numerical simulation of hypersonic boundary-layer instability with surface roughness," *Journal of Computational Physics*, Vol. 229, No. 19, 2010, pp. 7207–7237.

[9]Fong, K. D., Wang, X., and Zhong, X., "Numerical simulation of roughness effect on the stability of a hypersonic boundary layer," *Computers and Fluids*, Vol. 96, 2014, pp. 350–367.

[10]Fong, K. D., Wang, X., and Zhong, X., "Stabilization of hypersonic boundary layer waves using 2-D surface roughness," *43rd Fluid Dynamics Conference*, No. January, 2013, pp. 1–20.

[11]Fong, K. D., Wang, X., Huang, Y., Zhong, X., McKiernan, G. R., Fisher, R. A., and Schneider, S. P., "Second Mode Suppression in Hypersonic Boundary Layer by Roughness: Design and Experiments," *AIAA Journal*, Vol. 53, No. 10, 2015, pp. 1–6.

[12]Haley, C. and Zhong, X., "Direct Numerical Simulation of Hypersonic Flow over a Blunt Cone with Axisymmetric Isolated Roughness," *AIAA 2017-4514*, 2017.

[13]Zhong, X., "High-Order Finite-Difference Schemes for Numerical Simulation of Hypersonic Boundary-Layer Transition," *Journal of Computational Physics*, Vol. 144, No. 2, 1998, pp. 662–709.

[14]Malik, M. R., "Numerical methods for hypersonic boundary layer stability," *J. Comput. Phys.*, Vol. 86, No. 2, 1990, pp. 376–413.

[15]Casper, K. M., *Hypersonic Wind-Tunnel Measurements of Boundary-Layer Pressure Fluctuations*, Master's Thesis, Purdue University, School of Aeronautics & Astronautics, August 2009.

[16]Casper, K., Beresh, S., Henfling, J., Spillers, R., and Spitzer, S., "Hypersonic Fluid-Structure Interactions due to Intermittent Turbulent Spots on a Slender Cone," September 2018, Accepted for publication in AIAA Journal.

[17]Casper, K. M., Beresh, S. J., Henfling, J. F., Spillers, R. W., Pruett, B. O. M., and Schneider, S. P., "Hypersonic Wind-Tunnel Measurements of Boundary-Layer Transition on a Slender Cone," *AIAA Journal*, Vol. 54, No. 4, 2016, pp. 1250–1263.

[18]Fedorov, A. V. and Tumin, A., "High-speed boundary-layer instability: old terminology and a new framework," *AIAA Journal*, Vol. 49, No. 8, 2011, pp. 1647–1657.